

Article

The Nonlinear Dynamic Characteristics of an Industrial Turbine Engine with Eccentric Squeeze Film Dampers

Shan Zeng , Sigui Luo, Fei Wang ^{*}, Xifan Lan, Xinrui Ma and Yuxin Lu

School of Aircraft Engineering, Nanchang Hangkong University, Nanchang 330063, China; zengshan@nchu.edu.cn (S.Z.); lsg2606644068@163.com (S.L.); 13237689313@163.com (X.L.); maxinrui1016@163.com (X.M.); 18360946670@163.com (Y.L.)

* Correspondence: feiwang_1986@126.com

Abstract: Squeeze film dampers are often used to suppress vibration in turbine engines and play an important role in rotor systems. In this paper, the nonlinear dynamic characteristics of an industrial turbine engine fitted with squeeze film dampers are investigated with the static eccentricity of the SFDs. A recently developed time domain technique that combines the finite element method and the fixed interface modal synthesis method is applied to predict the nonlinear unbalance response of the industrial turbine engine under different unbalanced and static eccentricity configurations. By comparing the results obtained using SFDs with and without static eccentricity, it can be concluded that increasing the static eccentricity of the SFDs promotes non-periodic motion, while an increase in the unbalance level promotes the jump phenomenon. The efficiency of the rotor system would improve with an appropriate amount of unbalance applied to compressor IV, resulting in a reduction in the vibration level. If static sprung eccentricity occurs, the center of the journal orbit would be offset from the SFD center, rendering it inefficient or even leading to rub impact. Therefore, it is crucial to control the static eccentricity of the SFDs for optimal performance. The time domain technique is verified by the experimental results reported in the literature.



Citation: Zeng, S.; Luo, S.; Wang, F.; Lan, X.; Ma, X.; Lu, Y. The Nonlinear Dynamic Characteristics of an Industrial Turbine Engine with Eccentric Squeeze Film Dampers. *Appl. Sci.* **2023**, *13*, 13325. <https://doi.org/10.3390/app132413325>

Academic Editor: José António Correia

Received: 12 November 2023

Revised: 30 November 2023

Accepted: 7 December 2023

Published: 17 December 2023



Copyright: © 2023 by the authors. Licensee MDPI, Basel, Switzerland. This article is an open access article distributed under the terms and conditions of the Creative Commons Attribution (CC BY) license (<https://creativecommons.org/licenses/by/4.0/>).

Keywords: nonlinear vibration; SFD; modal synthesis method; eccentric; finite element method

1. Introduction

Squeeze film dampers (SFDs) are nonlinear elements used in aero-engine assemblies to attenuate vibrations and transmit forces. A retainer spring placed in parallel with the oil film is often used to support the gravity load on the journal. However, there are many practical situations where there is a significant degree of static eccentricity of the journal within the bearing housing, such as preloading errors, manufacturing errors, inappropriate assembly, or partial failures of the retainer spring in service. This offset results in nonlinearity that is evident by the presence of nonsynchronous frequency components in the vibration. This paper deals with sprung eccentricity.

Many researchers have attempted to obtain the nonlinear response of eccentric SFD-supported rotor systems. Tonnesen [1] studied the unbalance response of an eccentric squeeze-film-damper-mounted rigid rotor, experimentally and theoretically. An offset synchronous and elliptic orbit was observed in experiments, and a perturbation method was applied to obtain the nonlinear response. Sykes and Holmes [2] also conducted an experimental study on a rotor system supported on squeeze film dampers with static misalignment. Subharmonic motions were observed and attributed to the static misalignment of the squeeze film damper. Zhao et al. [3] investigated the stability of eccentric-squeeze-film-damper-mounted rotor systems with a trigonometric collocation method. It was found that nonsynchronous vibration and jump phenomena might arise if the parameters of the eccentric squeeze film damper are inappropriate. Bonello [4] studied the cavitated eccentric SFD model with the receptance harmonic balance (RHB) method. The study focused

on the effects of cavitation and found that cavitation might be beneficial in preventing excessive vibration of the shaft. Recent experimental investigations [5] showed that the critical speed of the rotor system might increase due to the static eccentricity of the squeeze film damper, and the theoretical prediction based on short bearing approximation showed some consistency with the experimental data. Deng et al. [6] developed a non-contact method to identify the unbalanced mass of a rotor system in 3D space. In comparison with sensor methods, the relative error of the proposed method decreased from 30.6% and 41.3% to 2.2%.

Although much work has been conducted, it can be seen that most of the studies were conducted with rigid rotor systems or simple flexible rotor systems. Additionally, to alleviate the computational burden, most of the theoretical investigations adopted frequency domain techniques, such as the harmonic balance method or trigonometric collocation method. However, as stated in Reference [4], these techniques might yield results that disagree with the numerical integration method due to a loss of periodicity. In comparison, time domain techniques yield the actual steady-state response after the initial transients have died out. All these facts necessitate that more effort should be made to improve the efficiency of the time domain techniques and thus enable more detailed models of a flexible rotor system mounted with sprung eccentric squeeze film dampers to be established and analyzed.

The time domain methods for the nonlinear unbalance response of rotor systems have been extensively investigated. Glasgow [7] employed the fixed interface modal synthesis method to reduce the size of the rotor system to obtain better computational efficiency. In References [8,9], the transfer matrix method was adopted. Wang, W. [10] improved the free interface modal synthesis method to analyze the dynamic characteristics of a multi-rotor system. Hsiao-Wei [11] established a dual-rotor system with the finite element method to investigate the influences of the speed ratio of the rotor system. Ma [12] analyzed the vibration attenuation effects of the SFD parameters selected by using the multi-objective optimization method on the dynamic response. Wang [13] investigated numerically the vibration responses of the rotor system under different rotating speeds and with different unbalances, and they compared and analyzed the influence of SFD on the vibration of the rotor system and the change in suppression capability. From all the above references, it can be seen that the component modal synthesis method is commonly applied to improve the efficiency of the time domain method.

Mohammed [14] studied the effect of bearing stiffness nonlinearity on the system dynamics when supported by stiff and soft linear bearings by means of the harmonic balance method and a continuation scheme. Nan et al. [15] established a new nonlinear rotor model supported by a rolling bearing. Zhang et al. [16] proposed a nonlinear model of a multi-disk rigid rotor with looseness and cubic nonlinear supporting and discussed the individual and coupling effects of these two nonlinearities on the transient and steady-state responses. Wang [17] considered the preload condition, surface waviness, Hertz contact and elastohydrodynamic lubrication to study an improved nonlinear dynamic model of rotor systems supported by angular contact ball bearings. Zharilkassin et al. [18], using Bogolyubov's asymptotic method and numerical methods, constructed a gyroscopic rigid unbalanced rotor with nonlinear cubic damping and nonlinear rigidity of the elastic support. Li et al. [19] studied the dynamic characteristics of an asymmetric rotor system supported by axial-grooved gas-lubricated bearings by using the hybrid numerical model.

In the present work, the finite element method and the fixed interface modal synthesis method are combined to model the flexible rotor system of an industrial turbine engine mounted with eccentric squeeze film dampers. Then, with this nonlinear model and the improved Newmark- β method, the nonlinear dynamic characteristics of the rotor system, with and without static eccentricity, are obtained, analyzed and compared.

2. Theoretical Modeling

2.1. Nonlinear Forces of the SFD

A recent experimental investigation [5] has demonstrated that the short bearing approximation of the SFD shows some consistency with experimental data. Therefore, the short bearing assumption is adopted in this work to incorporate the SFD with the rotor system. The nonlinear forces of the SFD are given in [20,21]:

$$\begin{cases} f_x^{sfd} = -\frac{\mu_s RL^3}{c^2(x^2+y^2)^{1/2}} \left[x(\dot{\varepsilon}I_2 + \varepsilon\dot{\psi}I_1) - y(\dot{\varepsilon}I_1 + \varepsilon\dot{\psi}I_3) \right] \\ f_y^{sfd} = -\frac{\mu_s RL^3}{c^2(x^2+y^2)^{1/2}} \left[y(\dot{\varepsilon}I_2 + \varepsilon\dot{\psi}I_1) + x(\dot{\varepsilon}I_1 + \varepsilon\dot{\psi}I_3) \right] \end{cases} \quad (1a)$$

$$\varepsilon = \sqrt{x^2 + y^2}/c \quad (1b)$$

$$\dot{\varepsilon} = (x\dot{x} + y\dot{y}) / \left(c\sqrt{x^2 + y^2} \right) \quad (1c)$$

$$\dot{\psi} = (y\dot{x} - x\dot{y}) / \left(x^2 + y^2 \right) \quad (1d)$$

$$\tan \psi = y/x. \quad (1e)$$

x is the horizontal displacement of the journal, and y denotes the vertical displacements. I_j ($j = 1, 2, 3$) denotes the Sommerfeld integrals. c is the radial clearance. μ_s denotes the dynamic viscosity of the film of the SFD. L and R are the length and radius of the SFD, respectively.

2.2. Equations of Motion and Numerical Algorithm

Using the finite element method, the equation of motion of the nonlinear rotor system can be expressed as shown below:

$$M\ddot{u} + G\dot{u} + Ku = F^{nonl} + F^{unb}, \quad (2)$$

M , K and G can be easily obtained using the finite element method. F^{nonl} denotes the nonlinear forces exerted by the SFD. F^{unb} denotes the unbalance force vector.

The model consists of second-order nonlinear differential equations. The computational efficiency depends on both the numerical methods used and the total degrees of freedom of the rotor system. To strike a balance between accuracy and computational efficiency, fixed interface modal synthesis is utilized to reduce the dimensionality of the model and therefore its computational effort.

Equation (2) can be rewritten as:

$$\begin{bmatrix} M_{II} & M_{IJ} \\ M_{JI} & M_{JJ} \end{bmatrix} \begin{bmatrix} \ddot{u}_I \\ \ddot{u}_J \end{bmatrix} + \begin{bmatrix} G_{II} & G_{IJ} \\ G_{JI} & G_{JJ} \end{bmatrix} \begin{bmatrix} \dot{u}_I \\ \dot{u}_J \end{bmatrix} + \begin{bmatrix} K_{II} & K_{IJ} \\ K_{JI} & K_{JJ} \end{bmatrix} \begin{bmatrix} u_I \\ u_J \end{bmatrix} = \begin{bmatrix} F_I^{unb} \\ 0 \end{bmatrix} + \begin{bmatrix} 0 \\ F_J^{nonl} \end{bmatrix}, \quad (3)$$

where u_I is the linear DOFs where only unbalance forces act, while u_J represents the non-linear DOFs or the interface of DOFs in this work.

A detailed description of the modeling and solving process can be found in Reference [21].

$$q_k^{n+1} = S_q^{-1} \left(\phi_k^T F_I^{unb \ n+1} - V_q u_J^{n+1} + W_q \right) \quad (4a)$$

$$(S_J - V_J S_q^{-1} V_q) u_J^{n+1} = F_J^{nonl \ n+1} + (\phi_c^T - V_J S_q^{-1} \phi_k^T) F_I^{unb \ n+1} - V_J S_q^{-1} W_q + W_J, \quad (4b)$$

with

$$W_q = \overline{M}_{II} A_q^n + \overline{G}_{II} B_q^n + \overline{M}_{IJ} A_J^n + \overline{G}_{IJ} B_J^n \quad (5a)$$

$$W_J = \bar{M}_{JJ} A_J^n + \bar{G}_{JJ} B_J^n + \bar{M}_{JI} A_q^n + \bar{G}_{JI} B_q^n \quad (5b)$$

$$S_q = a\bar{M}_{II} + b\bar{G}_{II} + \bar{K}_{II} \quad (5c)$$

$$S_J = a\bar{M}_{JJ} + b\bar{G}_{JJ} + \bar{K}_{JJ} \quad (5d)$$

$$V_q = a\bar{M}_{IJ} + b\bar{G}_{IJ} \quad (5e)$$

$$V_J = a\bar{M}_{JI} + b\bar{G}_{JI} \quad (5f)$$

$$F_J^{nonl\ n+1} = F_J^{nonl\ n}(u_J^{n+1}, \dot{u}_J^{n+1}). \quad (5g)$$

In summary, the nonlinear model of the rotor system is established using the fixed interface modal synthesis method and the finite element method; then, an implicit time domain method based on the Newmark β method is applied to solve the equations of motion of the reduced system so that the dynamic characteristics can be obtained.

3. Numerical Results and Discussion

3.1. Model Introduction

The industrial turbine engine studied in this paper is shown in Figure 1a. A is SFD I, and B is SFD II. The coordinate system is shown in Figure 1b, where s , ox , oz are horizontal axes and oy is a vertical axis.

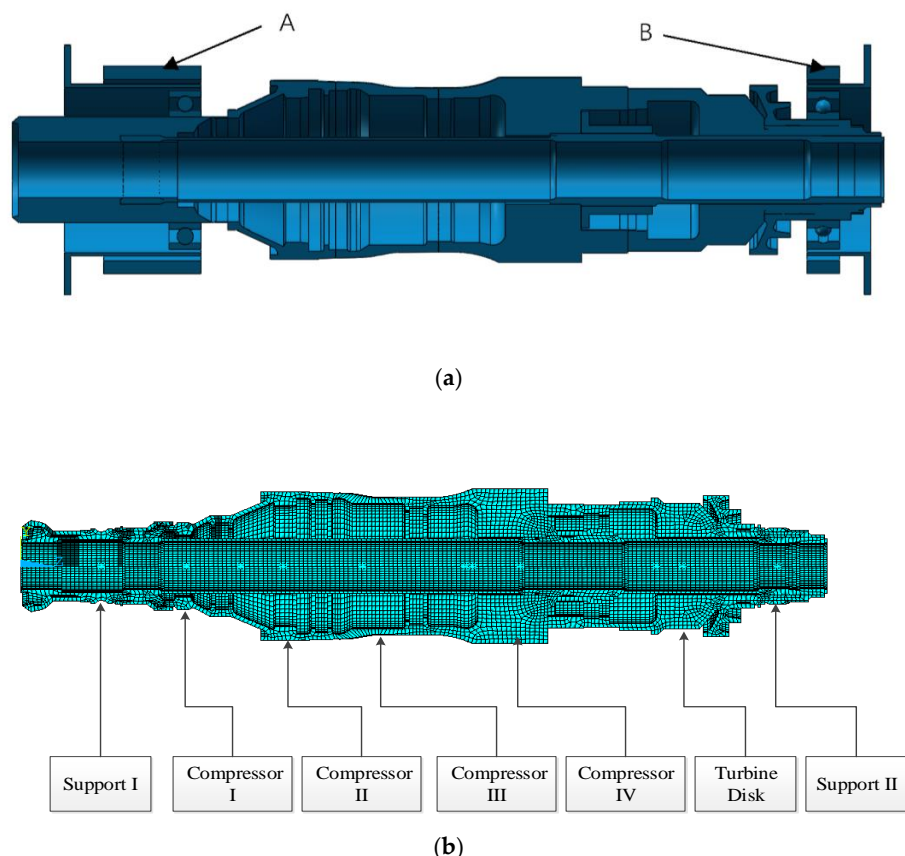


Figure 1. *Cont.*

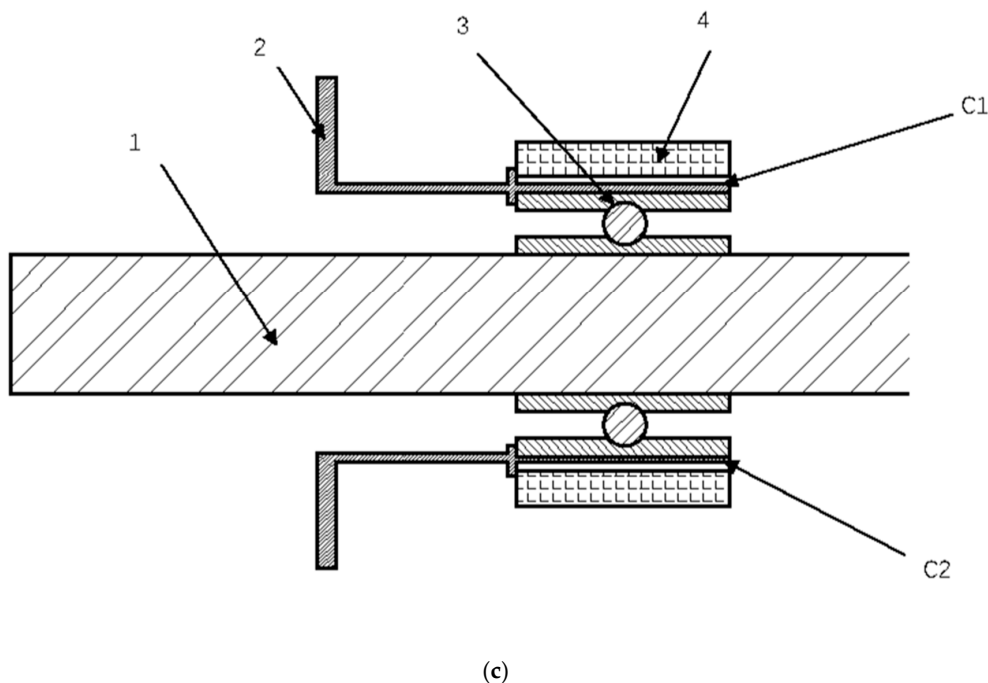


Figure 1. Model diagram: (a) structural diagram of the industrial turbine engine; (b) cross-section of the industrial turbine engine; (c) structure diagram of the SFD.

The structure of the SFD is shown in Figure 1c. 1 is the shaft; 2 is the squirrel cage; 3 is the bearing; 4 is the bearings bracket. C1 and C2 denote the oil film gap. When $C1 \neq C2$, it means that the rotor system has static eccentricity.

The industrial turbine engine is a single rotor system. It includes two supports and five disks. The front and rear supports of the rotor system are supports I and II, respectively. The squirrel cage + rolling bearing + SFD support scheme is adopted for supports I and II. The five disks comprise three stages: the axial compressor—compressors I, II and III, one centrifugal compressor—compressor IV, and one turbine. The operating range for the engine is 0–4712 rad/s and the continuous operating speed is 3665 rad/s.

Model parameters of the rotor system are listed in Tables 1–3. Stiffness coefficients of the elastic supports are listed in Table 1. The parameters of the SFDs are listed in Table 2. The inertia properties of the blades for each disk are listed in Table 3.

The Young's modulus of the turbine disk is 176 GPa, and the mass density is 8300 kg/m^3 . For the rest of the rotor system, the Young's modulus is 196 GPa, and the mass density is 7810 kg/m^3 . The 40 modes in the normal modal matrix ϕ_k were retained for the application of the modal synthesis method. For the Newmark- β method, $\alpha = 0.25$ and $\beta = 0.5$.

Table 1. Stiffness of elastic supports (squirrel cage) in industrial turbine engine.

	Support I	Support II
Stiffness (N/m)	1.92×10^7	2.75×10^7

Table 2. Parameters of SFDs in industrial turbine engine.

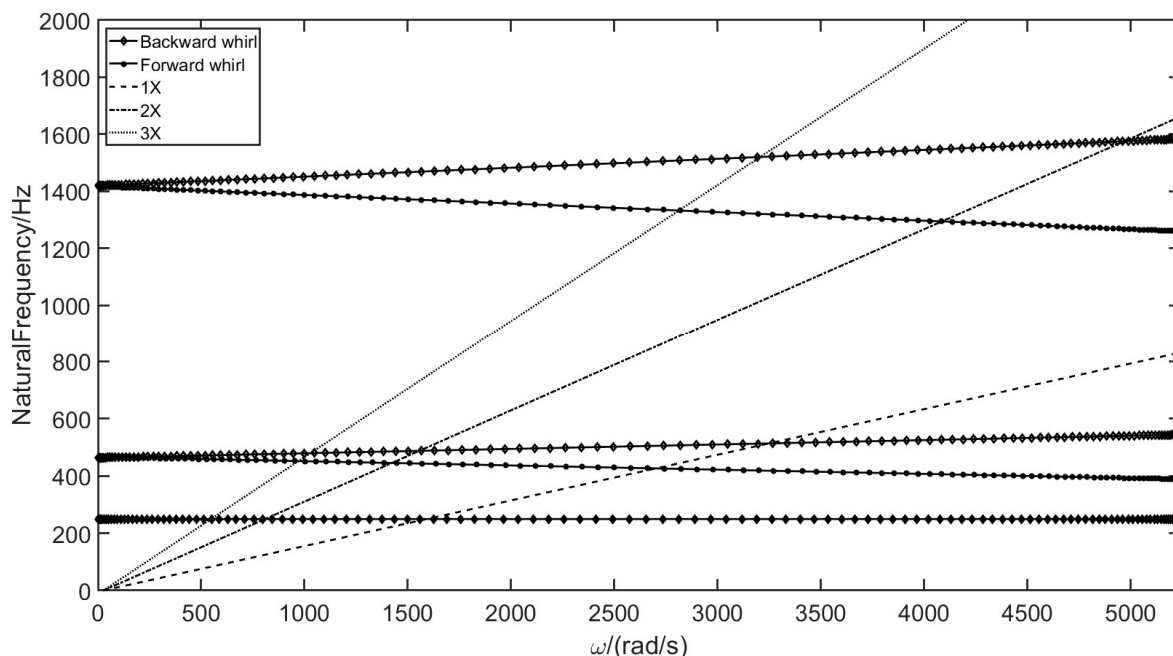
	SFD I	SFD II
Radius R/mm	39.00	38.75
Length L/mm	20.30	7.20
Radial clearance c/mm	0.07	0.09
Dynamic viscosity $\mu\text{s}/10^{-3}\text{Pa}\cdot\text{s}$		5.12

Table 3. Inertia properties of blades for each disk.

	Compressor I	Compressor II	Compressor III	Compressor IV	Turbine
Mass (kg)	0.17	0.36	0.28	1.269	2.12
Polar moment of inertia ($\times 10^{-3}$ kg·m 2)	4.35	1.15	0.79	9.03	10.00

3.2. Critical Speeds Analysis

The Campbell diagram of the rotor system is presented in Figure 2. Two critical speeds, 1588 rad/s and 3276 rad/s, can be identified from the Campbell diagram. The corresponding mode shapes for the critical speeds are shown in Figure 3. From Figure 3, it can be seen that the first mode, Figure 3a, is a cylindrical mode, while the second one, Figure 3b, is a conical mode. Furthermore, Figure 3 implies that the rear end of the rotor would have a greater amplitude of vibration than the front end when passing through the first critical speed, while the reverse is true when passing through the second one.

**Figure 2.** Campbell diagram of the rotor system.**Figure 3.** Mode shapes of the first two critical speeds: (a) mode shape for critical speed 1588 rad/s; (b) mode shape for critical speed 3276 rad/s.

3.3. Without Sprung Eccentricity

With the method described in Section 2, the finite element model of the rotor system is established with 189 beam elements to simulate the shaft and 5 mass elements to simulate the blades of each disk. Then, the steady-state unbalance response of the rotor system

is obtained when the rotor speed is in the range of 1000–4500 rad/s and the step size is 10 rad/s. The first step uses zero initial conditions. The remaining steps use the results of the previous step as the initial conditions.

Figures 4–7 present the bifurcation diagram, the waterfall diagram and the frequency response of the rotor system without static sprung eccentricity under different unbalanced configurations. Here, $e_i, i = 1, 2, 3, 4, 5$ represent the eccentric distance of compressors I, II, III, IV and the turbine disk respectively. Thus, the unbalanced force on the rotor would be the mass of the disk $\times e_i \times$ square of the rotor speed. Also, the unbalance is applied to only one disk each time. For each disk, 10 different unbalanced configurations were considered with $e_i = 0.1, 0.2, 0.3 \dots 0.9, 1.0$ mm. However, it was found that the results were quite similar if e_1, e_2 and e_3 had adopted the same value, which is the same for e_4 and e_5 . Therefore, only the results of e_2 and e_4 are presented and analyzed in this work.

The following conclusions can be reached from Figures 4–7:

- (1) From Figure 4, the bifurcation diagrams of support I, it can be seen that although the unbalanced configurations are different, the rotor executes periodic motion with period one in 1000–4500 rad/s.
- (2) Figure 4d shows an obvious break point at 3250 rad/s while the dots in Figure 4a–c form an almost continuous curve. The break point implies the occurrence of a jump phenomenon caused by the nonlinear interaction between the rotor and the SFD. By examining Figures 5d and 6f, the waterfall diagram and the frequency response curve corresponding to Figure 4d, it is confirmed that the jump phenomenon does occur at 3250 rad/s for $e_4 = 1.0$ mm.
- (3) Increasing e_i would lead to a larger response, although the relationship between e_i and the response is nonlinear, as shown in Figure 7. Also, by comparing Figure 5a,b, it can be found that as e_i increases from 0.1 to 1 mm, the response of support I increases by approximately five times. The same phenomenon can also be observed in Figure 5c,d or Figure 6a,b.
- (4) Due to the nonlinearity of the SFD, the rotational speed at which the peak response occurs can be different from the critical speeds identified from the Campbell diagram, as shown in Figures 2 and 6. Two critical speeds, 1587 rad/s and 3274 rad/s, can be identified from the Campbell diagram shown in Figure 2. However, in Figure 6a, it can be seen that the peak response of the rotor system occurs at 1610–1680 rad/s, which is very close to 1587 rad/s. Also, Figure 6a shows that at approximately 1600 rad/s, the vibration amplitude of the turbine disk is the largest while that of support I is the smallest, which means that the operating deflection shape of the rotor system at about 1600 rad/s coincides with the mode shape shown in Figure 3a. This is also the situation for 3000–3500 rad/s, as shown in Figures 3b and 6a.
- (5) The peak response speed range is related to the amount of unbalance, as shown in Figures 6 and 7. Figure 7 shows the horizontal response of support I under different unbalanced configurations. From Figure 7a, it can be seen that as e_2 increases from 0.1 to 1.0 mm, the corresponding peak response speed increases from 1600 to 2200 rad/s. By comparing Figure 6a,b, it can be seen that the peak response speed range shifts to 1800–2200 rad/s in Figure 6b, which is much larger than that shown in Figure 6a.
- (6) The jump phenomenon is closely related to the SFD and the amount of unbalance, as shown in Figures 6 and 7. From Figures 6c–h and 7b, it can be seen that the jump phenomenon occurs when $e_4 \geq 0.7$ mm.
- (7) The operating deflection shape of the rotor system under a continuous operating speed of 3663 rad/s is greatly influenced by the amount and the axial location of the unbalance, as shown in Figure 6a,c. Figure 6a, $e_2 = 0.1$ mm, shows not only that the vibration level of support I is larger than the other parts of the rotor system around 3600 rad/s but also that the operating deflection shape coincides with the second mode shape presented in Figure 3b. However, when $e_4 = 0.1$ mm, Figure 6c shows that the vibration level of support II is the largest around 3600 rad/s. By comparing Figure 6a,c, it can be seen that the vibration level of the rotor system at $e_4 = 0.1$ mm

is much smaller than that at $e_2 = 0.1$ mm. This indicates that the response of the rotor system is much more sensitive to the unbalance of compressor II compared to compressor IV.

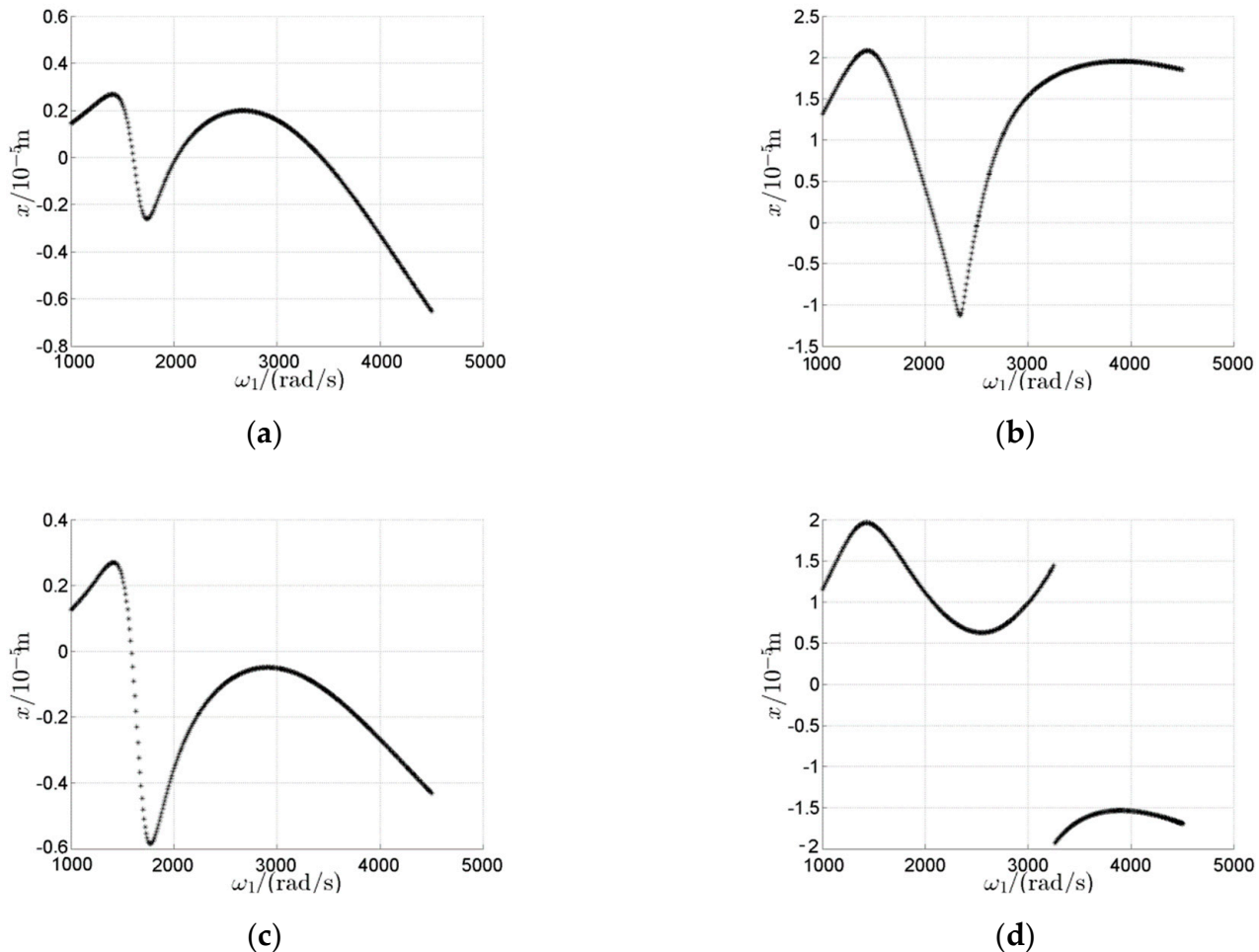


Figure 4. Bifurcation diagram of support I in 1000–4500 rad/s: (a) bifurcation diagram – $e_2 = 0.1$ mm; (b) bifurcation diagram – $e_2 = 1.0$ mm; (c) bifurcation diagram – $e_4 = 0.1$ mm; (d) bifurcation diagram – $e_4 = 1.0$ mm.

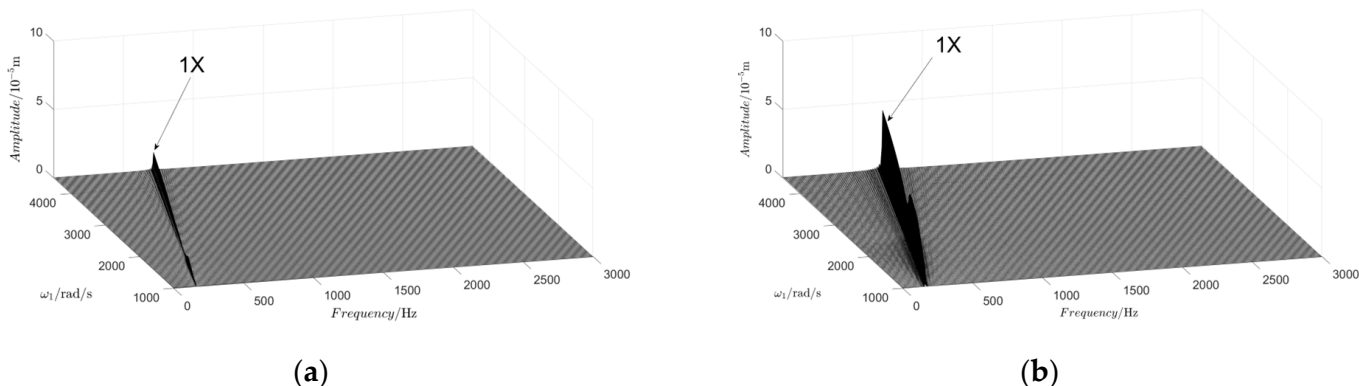


Figure 5. Cont.

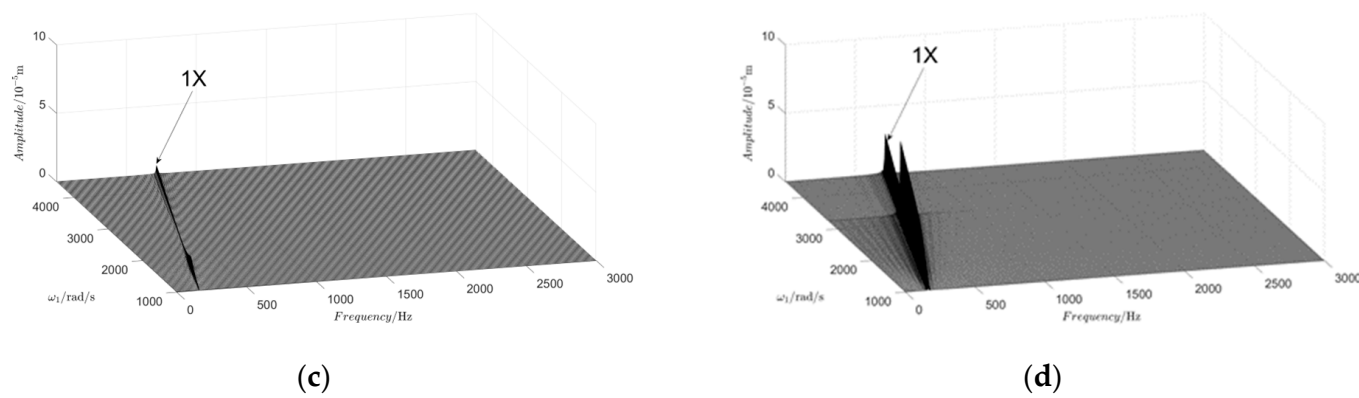


Figure 5. Waterfall diagram of support I in 1000–4500 rad/s: (a) waterfall diagram – $e_2 = 0.1 \text{ mm}$; (b) waterfall diagram – $e_2 = 1.0 \text{ mm}$; (c) waterfall diagram – $e_4 = 0.1 \text{ mm}$; (d) waterfall diagram – $e_4 = 1.0 \text{ mm}$.

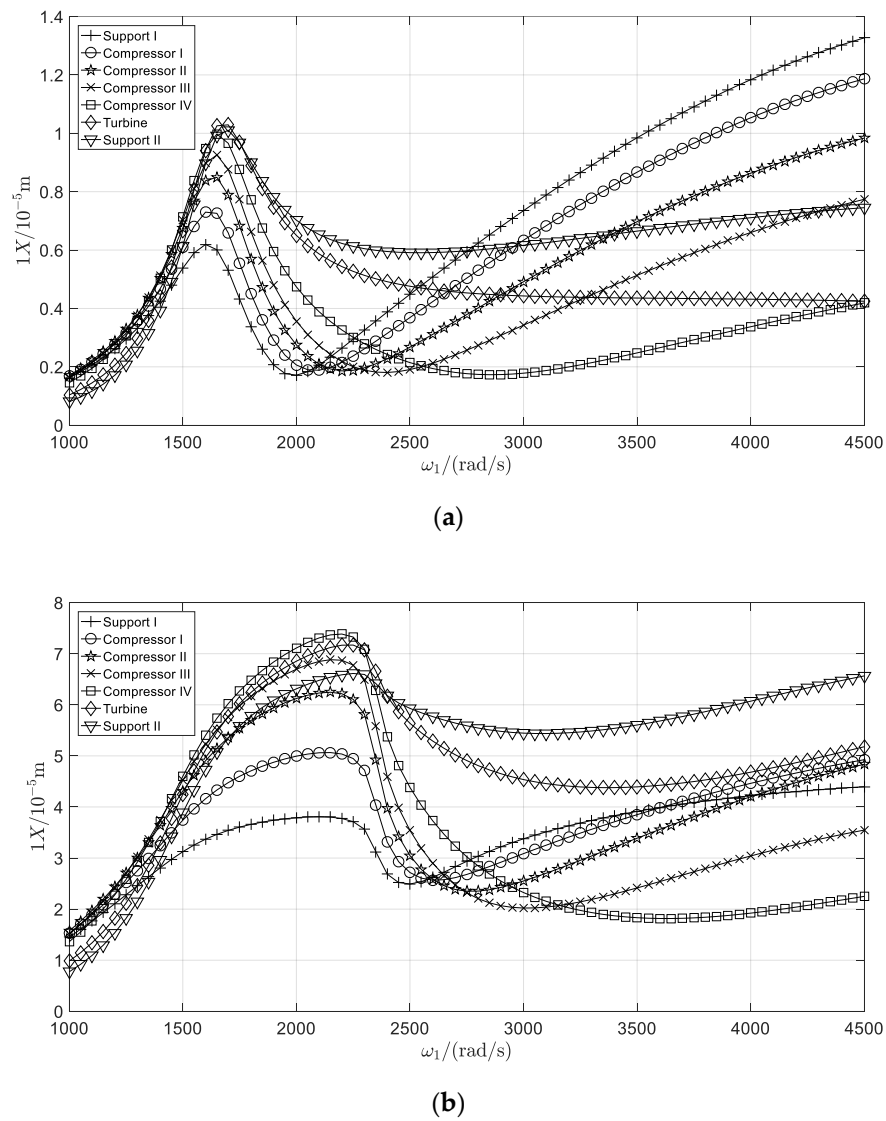
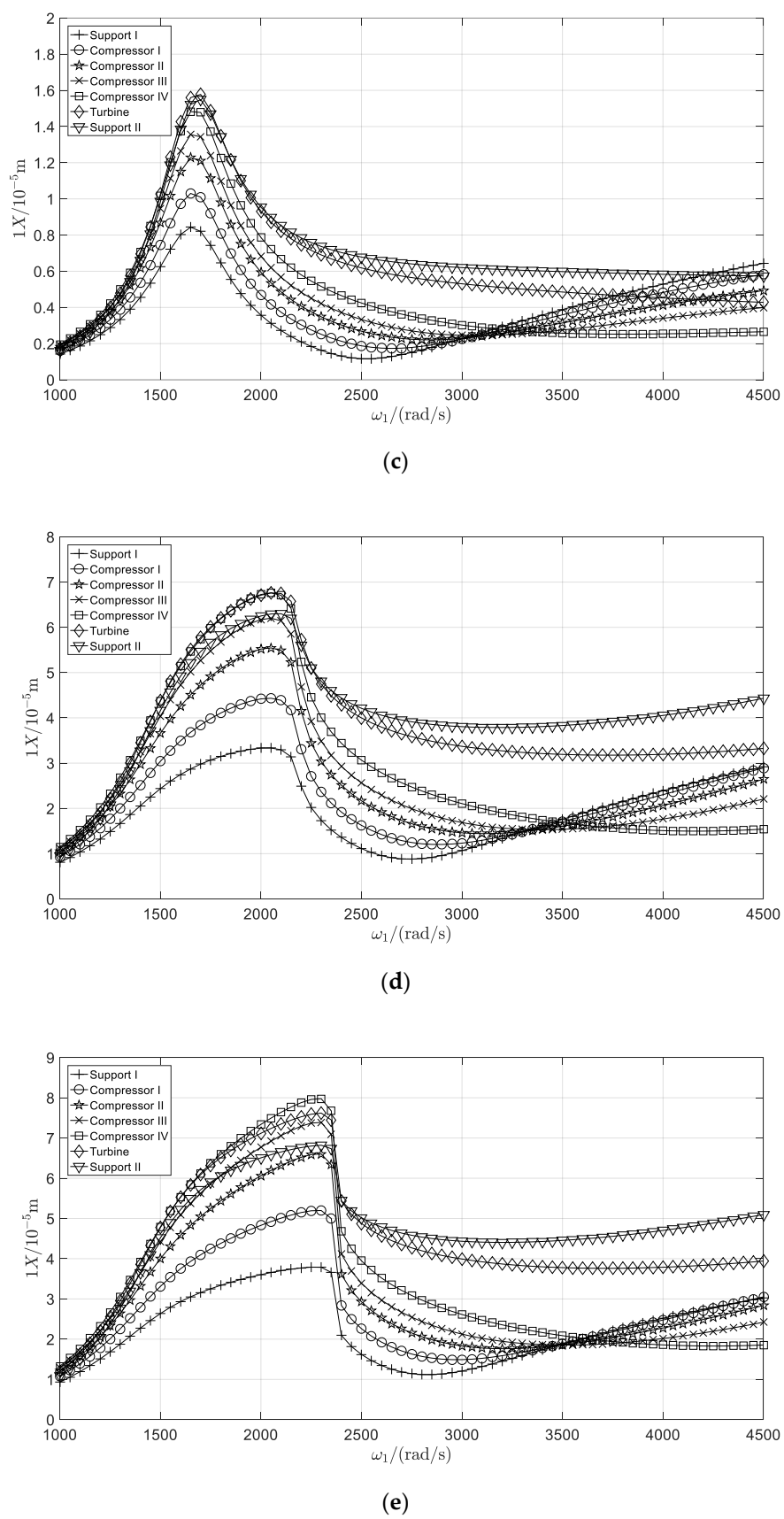
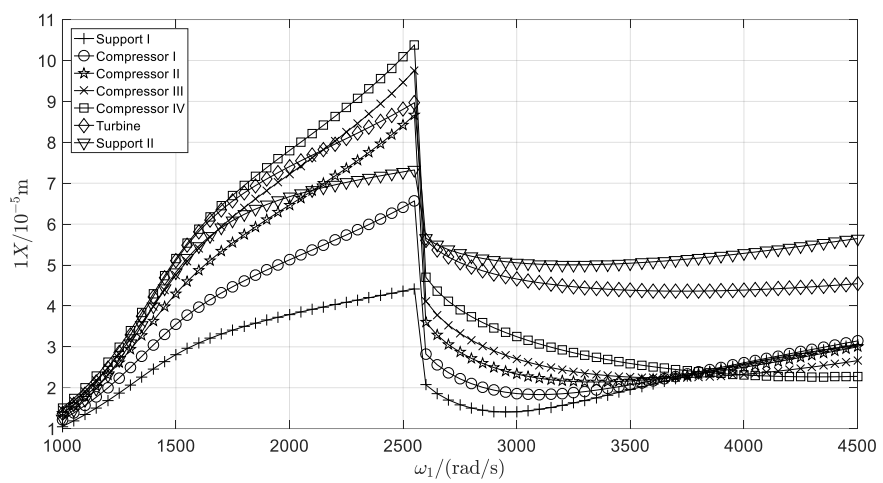
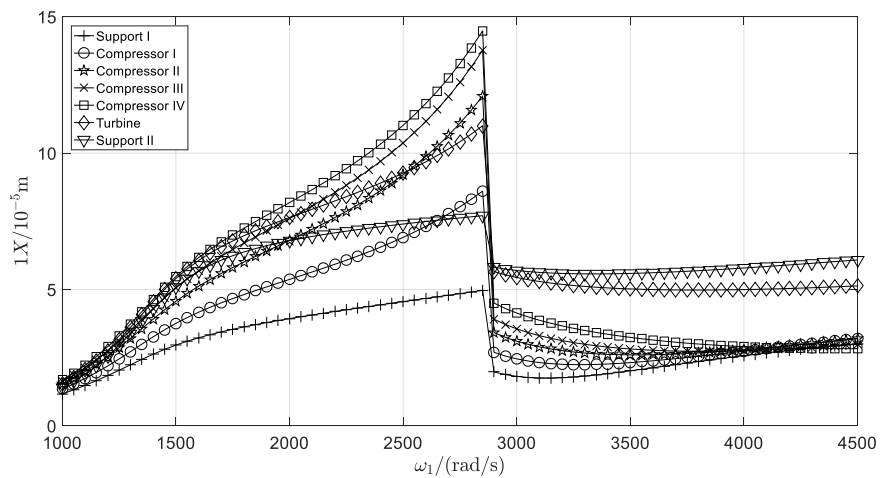


Figure 6. Cont.

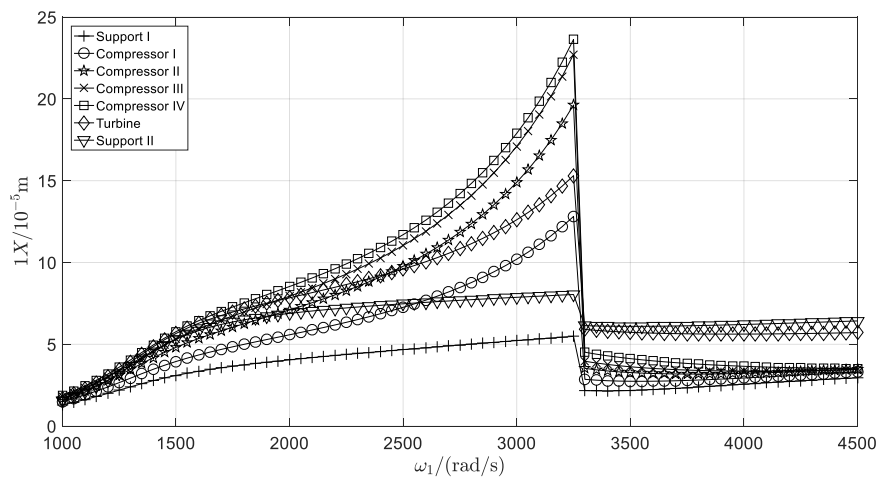
**Figure 6.** Cont.



(f)



(g)



(h)

Figure 6. Horizontal response of the rotor in 1000–4500 rad/s: (a) $e_2 = 0.1$ mm; (b) $e_2 = 1.0$ mm; (c) $e_4 = 0.1$ mm; (d) $e_4 = 0.6$ mm; (e) $e_4 = 0.7$ mm; (f) $e_4 = 0.8$ mm; (g) $e_4 = 0.9$ mm; (h) $e_4 = 1.0$ mm.

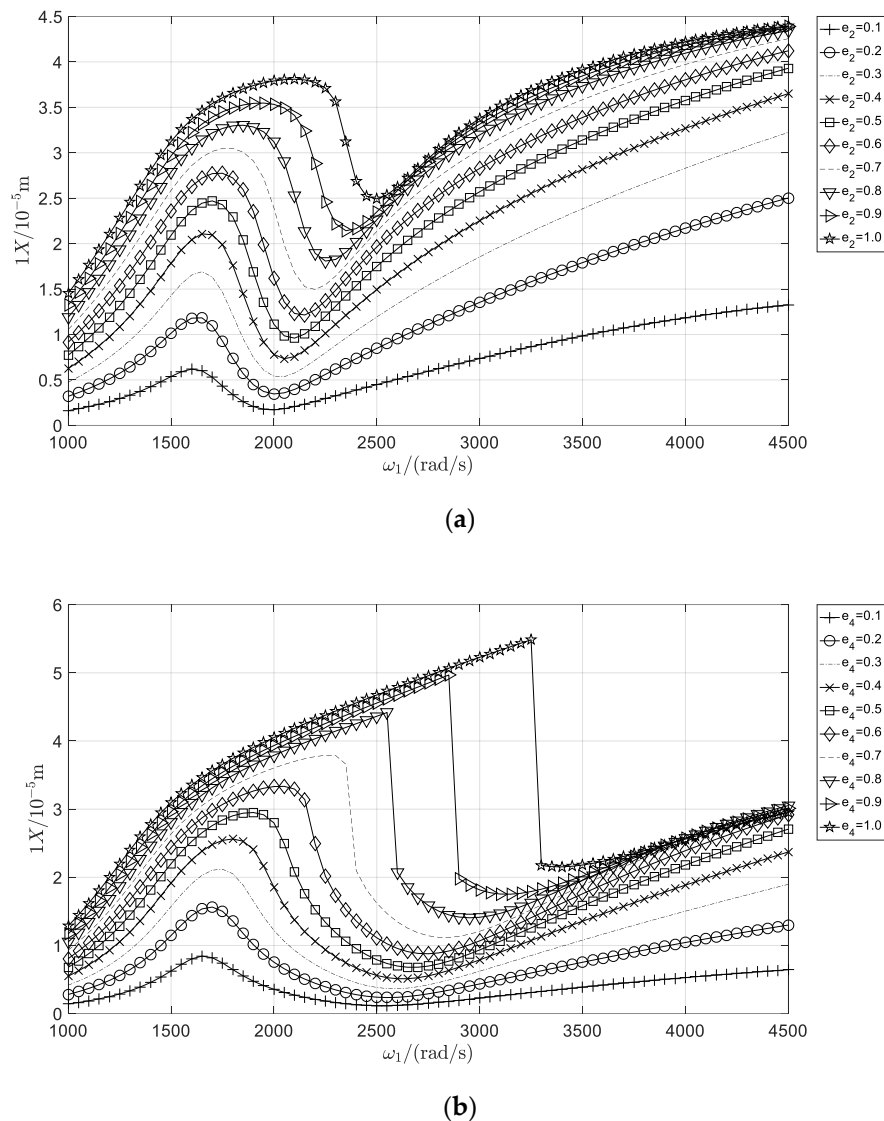


Figure 7. Horizontal response of support I in 1000–4500 rad/s under different unbalanced configuration: (a) $e_2 = 0.1 – 1.0$ mm; (b) $e_4 = 0.1 – 1.0$ mm.

3.4. The Influence of Sprung Eccentricity

In order to evaluate the influence of the static sprung eccentricity, the nonlinear dynamic characteristics of the rotor system under different static sprung eccentricities were computed and analyzed. The parameters for computation were the same as described in Section 3.3. The results are presented in Figures 8–15. In these figures, $e_{sx} = x_{01}/c_1$ is the normalized static sprung eccentricity for support I, in which x_{01} is the static offset in the x direction for support I and c_1 represents the radial clearance of the SFD for support I.

The following conclusions can be reached from Figures 8–15:

- (1) The periodicity of the motion of the rotor system is prone to be affected by the static sprung eccentricity, as shown in Figure 8. The bifurcation diagrams shown in Figure 8a,c,e,g suggest that for the same unbalanced configuration, quasi-periodic and chaotic motion are prone to occur at larger static sprung eccentricity. For the rotor system studied in this work, the operating speed regime within which the periodicity is strongly affected is 2500–3800 rad/s. Furthermore, by comparing Figure 8a–h, it can be seen that a larger unbalance would be beneficial in suppressing the non-periodic motion of the rotor system. Figure 8e shows an obvious bifurcation at 2800 rad/s, while Figure 8f indicates that the rotor system executes periodic motion in the whole

operating speed range. The same conclusion can also be reached by comparing Figure 8g,h.

- (2) The static sprung eccentricity would lead to the occurrence of the 0X and 2X frequency components in the waterfall diagram, as shown in Figure 9. This phenomenon has also been reported in Reference 4. Comparing Figure 5, Figure 9, it can be seen that the larger the static sprung eccentricity, the larger the amplitude of 0X, 1X and 2X. However, Figure 9g,h indicate that a larger unbalance would suppress the 0X component. Figure 9b,d,f,h also suggest that the 0X component would fluctuate under larger static sprung eccentricity.
- (3) The amplitude of the 1X component increases with an increasing amount of balance while that of the 0X component decreases, as shown in Figures 10–13. On the one hand, Figures 10a, 11a, 12a and 13a show that the amplitude of the 0X component decreases with an increasing amount of balance; on the other hand, by comparing these figures, it can be seen that the larger the static sprung eccentricity, the larger the amplitude of the 0X component. In Figure 10a, the maximum amplitude of the 0X component with $e_2 = 0.1\text{mm}$ and $e_{sx} = 0.1$ is approximately $1.4 \times 10^{-5}\text{ m}$; in Figure 12a, the maximum amplitude of the 0X component with $e_2 = 0.1\text{ mm}$ and $e_{sx} = 0.3$ is approximately $4.2 \times 10^{-5}\text{ m}$.

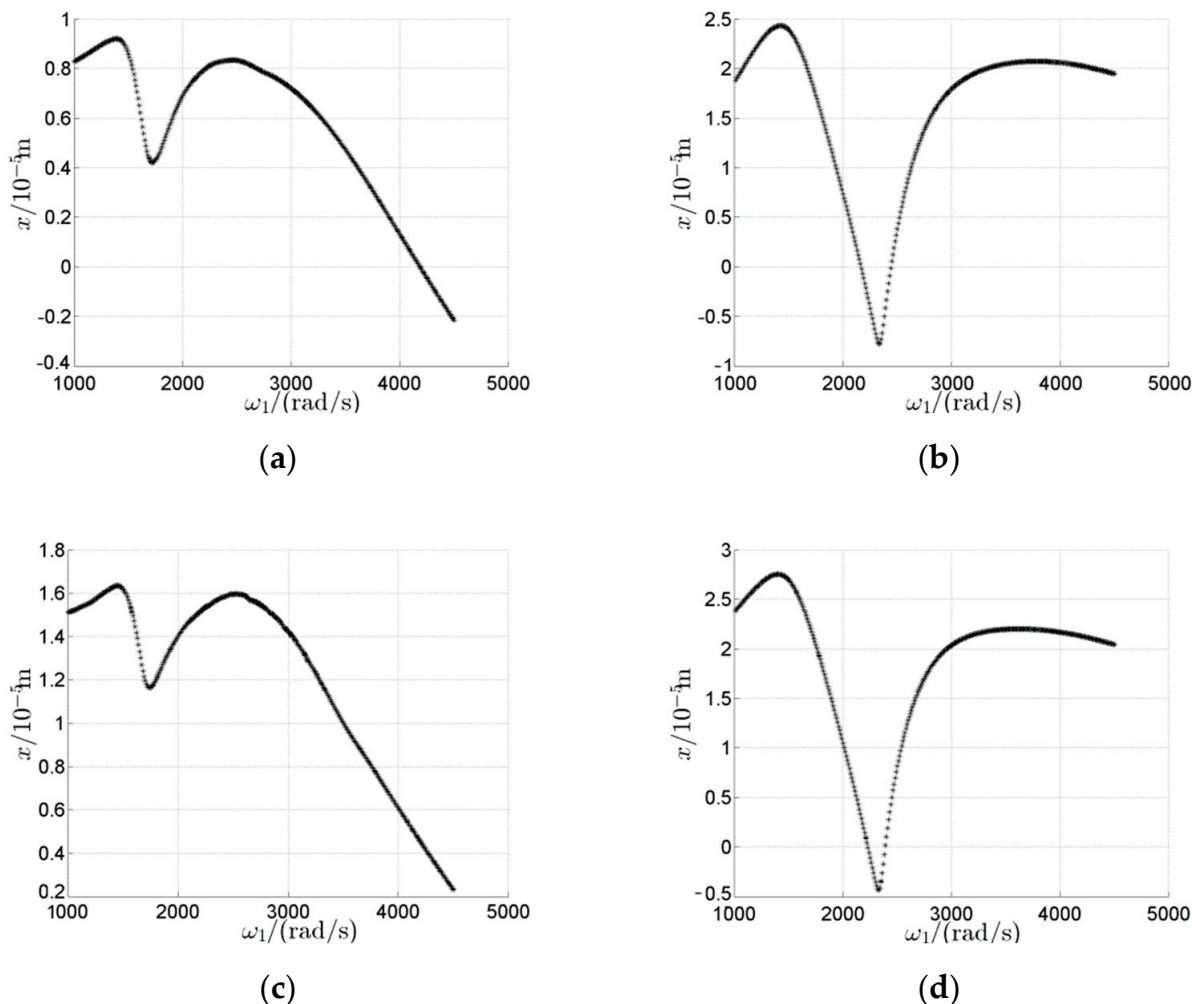


Figure 8. Cont.

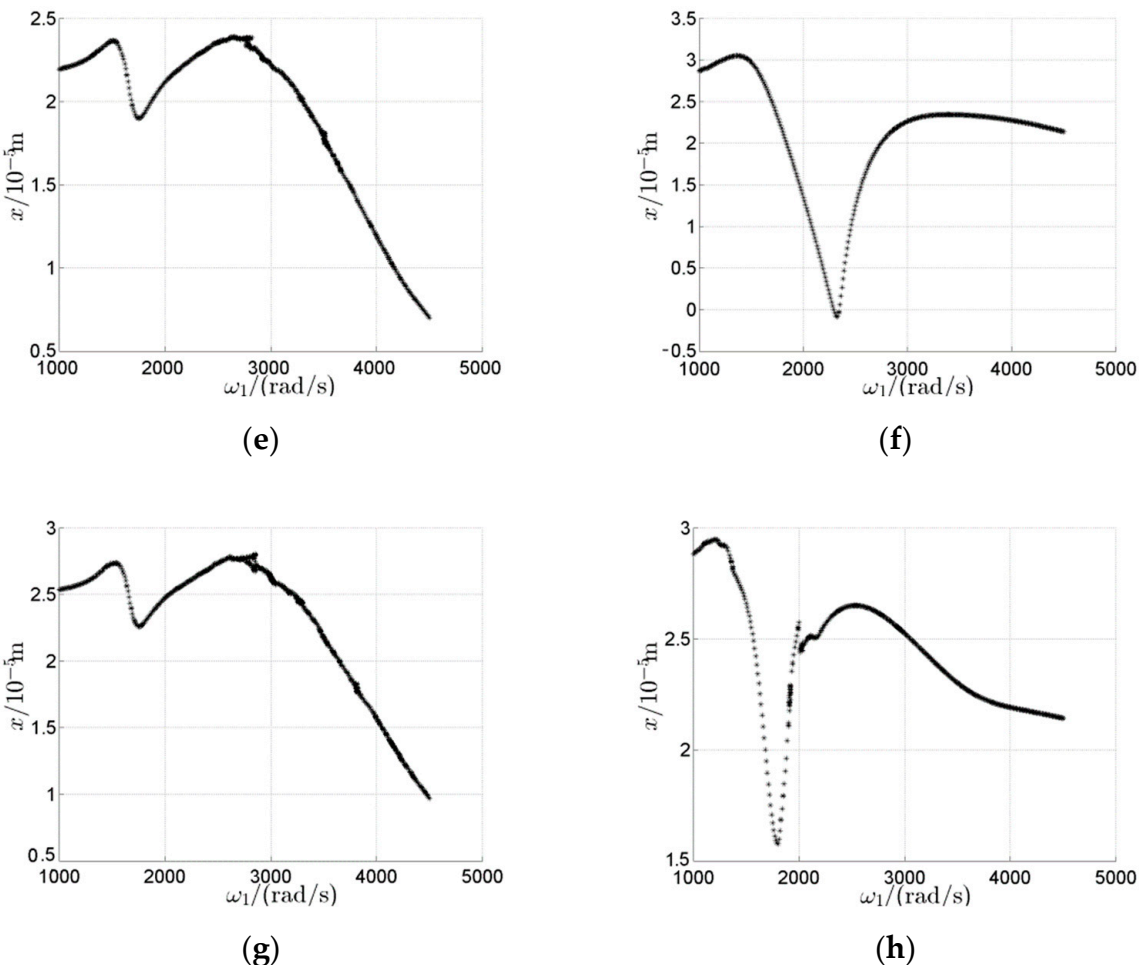


Figure 8. Bifurcation diagram of support I in 1000–4500 rad/s: (a) $e_2 = 0.1$ mm, $e_{sx} = 0.1$; (b) $e_2 = 1.0$ mm, $e_{sx} = 0.1$; (c) $e_2 = 0.1$ mm, $e_{sx} = 0.2$; (d) $e_2 = 1.0$ mm, $e_{sx} = 0.2$; (e) $e_2 = 0.1$ mm, $e_{sx} = 0.3$; (f) $e_2 = 1.0$ mm, $e_{sx} = 0.3$; (g) $e_2 = 0.1$ mm, $e_{sx} = 0.35$; (h) $e_2 = 1.0$ mm, $e_{sx} = 0.35$.

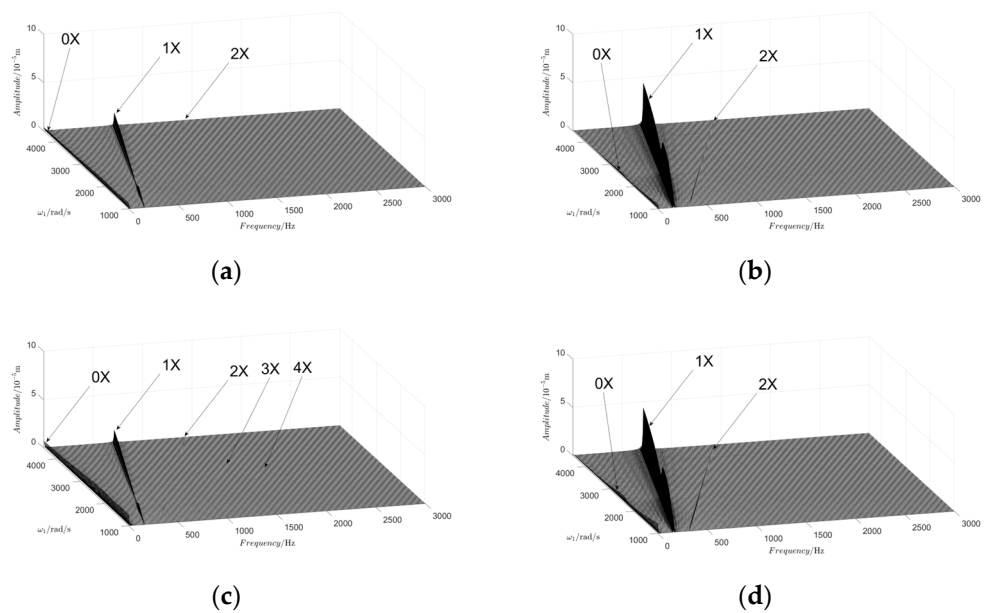


Figure 9. Cont.

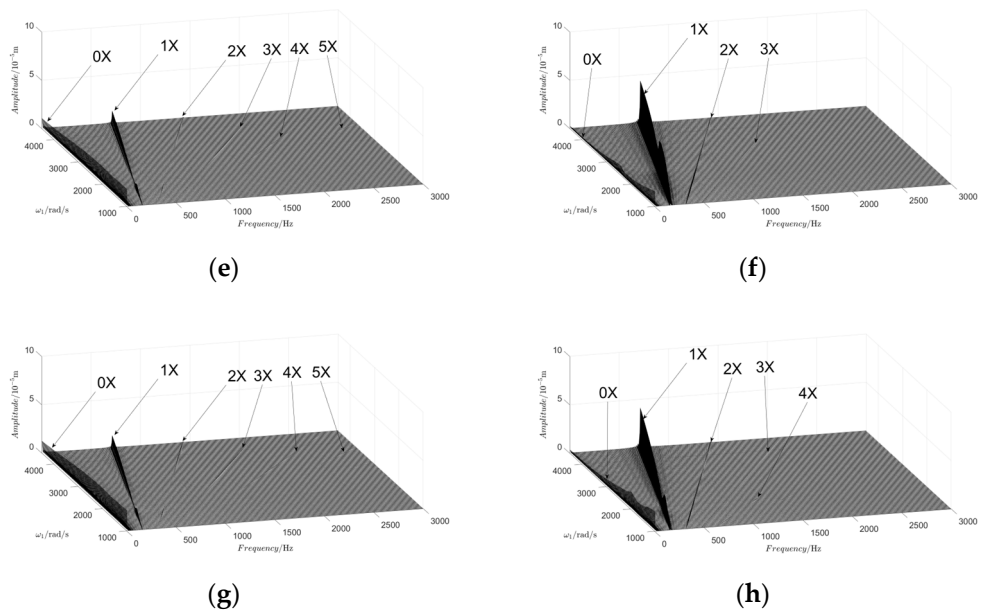


Figure 9. Waterfall diagram of support I in 1000–4500 rad/s: (a) $e_2 = 0.1$ mm, $e_{sx} = 0.1$; (b) $e_2 = 1.0$ mm, $e_{sx} = 0.1$; (c) $e_2 = 0.1$ mm, $e_{sx} = 0.2$; (d) $e_2 = 1.0$ mm, $e_{sx} = 0.2$; (e) $e_2 = 0.1$ mm, $e_{sx} = 0.3$; (f) $e_2 = 1.0$ mm, $e_{sx} = 0.3$; (g) $e_2 = 0.1$ mm, $e_{sx} = 0.35$; (h) $e_2 = 1.0$ mm, $e_{sx} = 0.35$.

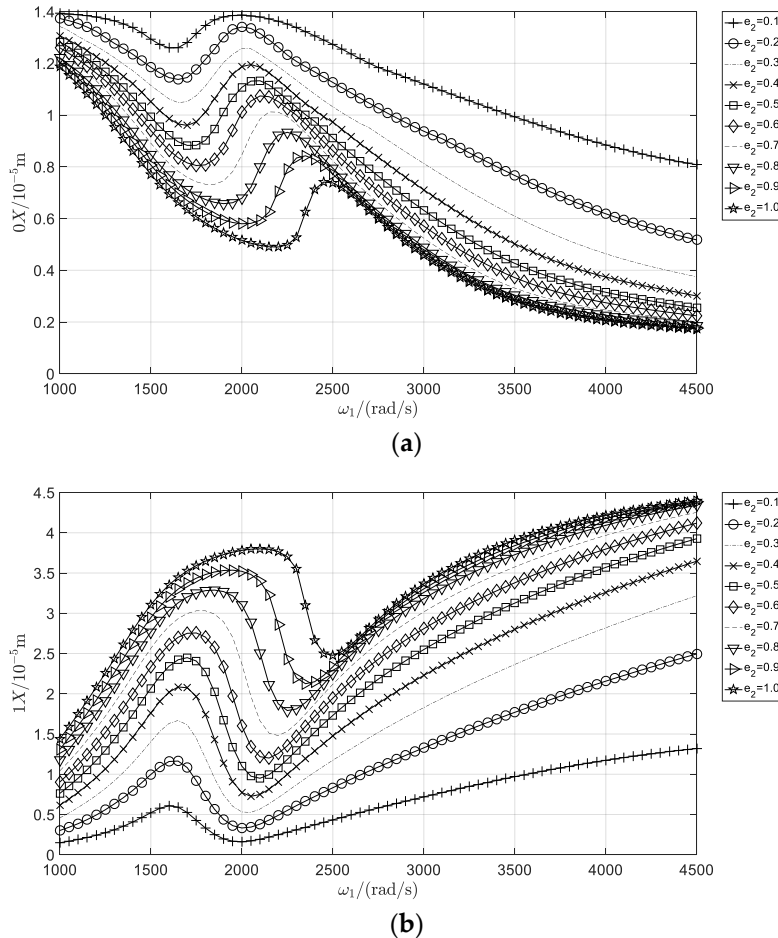


Figure 10. Horizontal response of support I in 1000–4500 rad/s with $e_2 = 0.1 – 1.0$ mm, $e_{sx} = 0.1$: (a) 0X; (b) 1X.

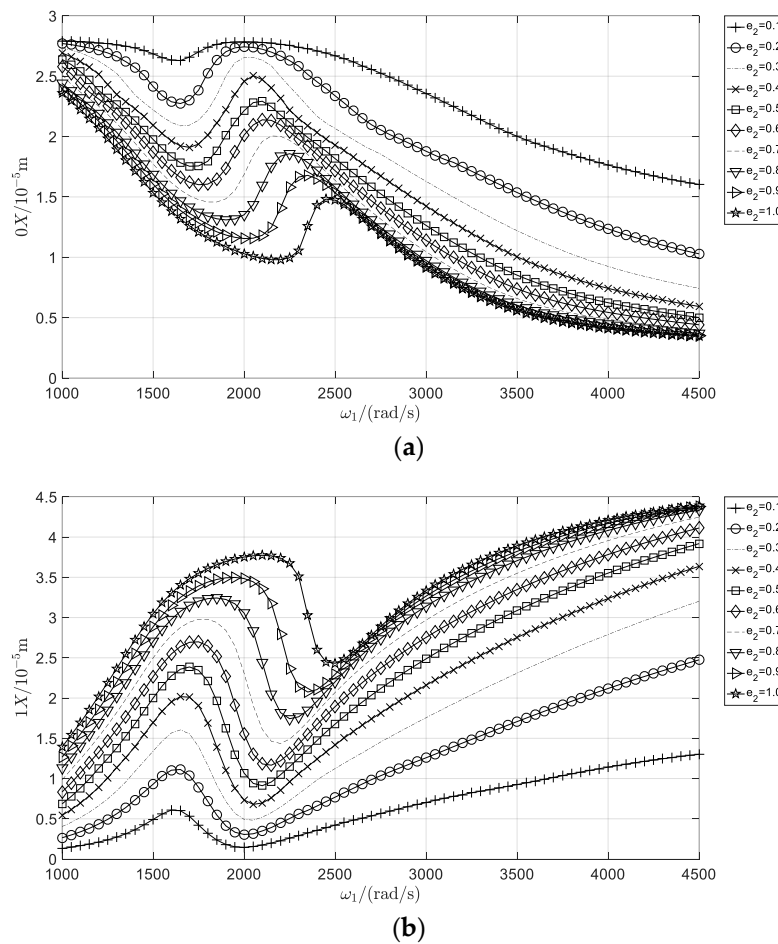


Figure 11. Horizontal response of support I in 1000–4500 rad/s with $e_2 = 0.1 – 1.0$ mm, $e_{sx} = 0.2$:
(a) $0X$; (b) $1X$.

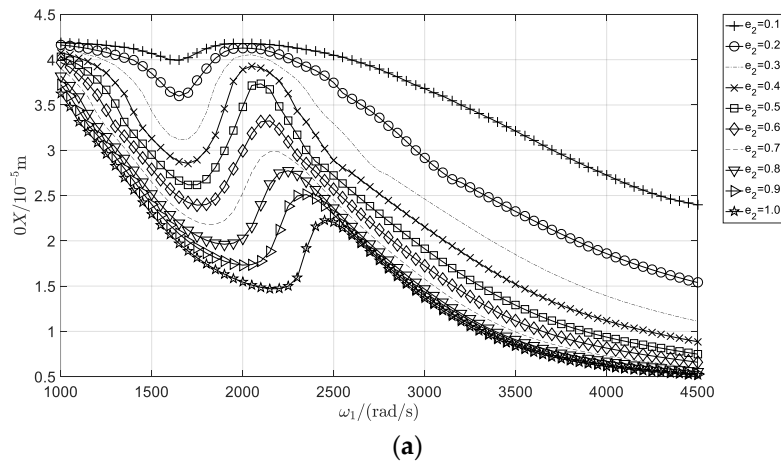


Figure 12. Cont.

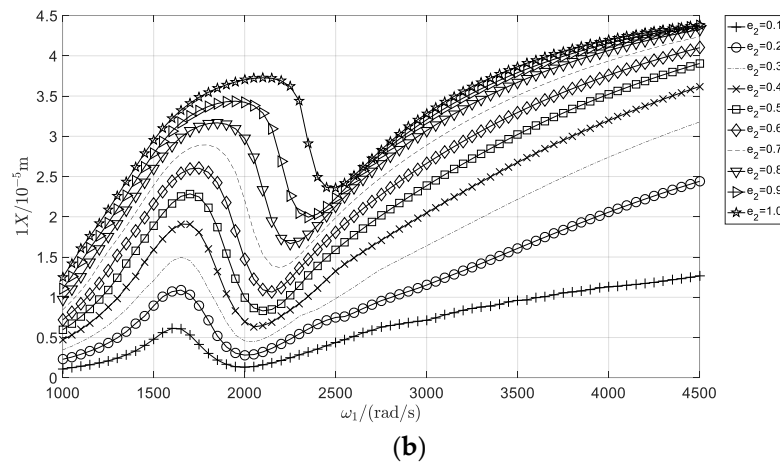


Figure 12. Horizontal response of support I in 1000–4500 rad/s with $e_2 = 0.1 - 1.0$ mm, $e_{sx} = 0.3$:
(a) 0X; (b) 1X.

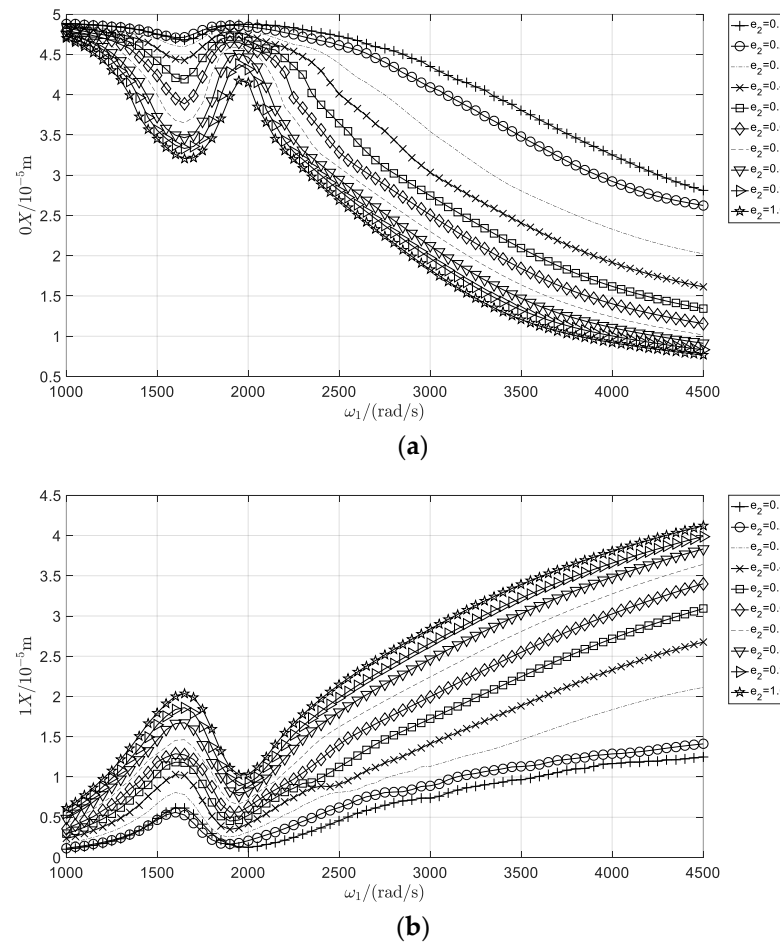


Figure 13. Horizontal response of support I in 1000–4500 rad/s with $e_2 = 0.1 - 1.0$ mm, $e_{sx} = 0.35$:
(a) 0X; (b) 1X.

- (4) Figure 14a indicates that the further the distance between the components of the rotor and the static eccentric SFD, the smaller the amplitude of the 0X frequency component. From Figure 14a, it can be seen that the amplitude of the 0X component for support II is the smallest, while that of support I is the largest. Figures 6a and 14b show that the operating deflection shape around 3665 rad/s coincides with the second mode shape shown in Figure 3b with and without static sprung eccentricity.

- (5) Due to the static sprung eccentricity, the center for the orbit of support I would be offset from the center of the SFD and thus make the SFD ineffective or even lead to the occurrence of rubbing impact, as shown in Figure 15a. Figure 15 presents the orbit and the spectrum of support I with $e_2 = 0.1$ mm, $e_{sx} = 0.35$ and $\omega_1 = 3600$ rad/s. It can be seen from Figure 15a,b that the amplitude of the orbit is much smaller than the static runout there, which means that the oil film was barely squeezed. In addition, 2X and 3X components can be observed in the spectrum.

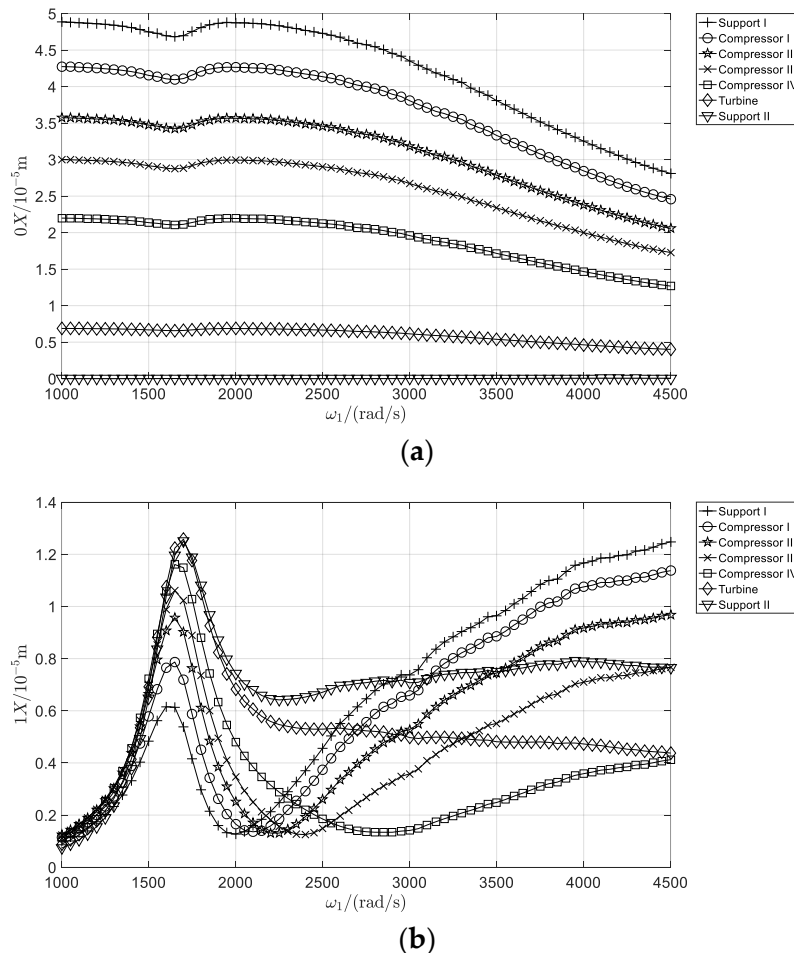


Figure 14. Horizontal response of the rotor system in 1000–4500 rad/s with $e_2 = 0.1$ mm, $e_{sx} = 0.35$: (a) 0X; (b) 1X.

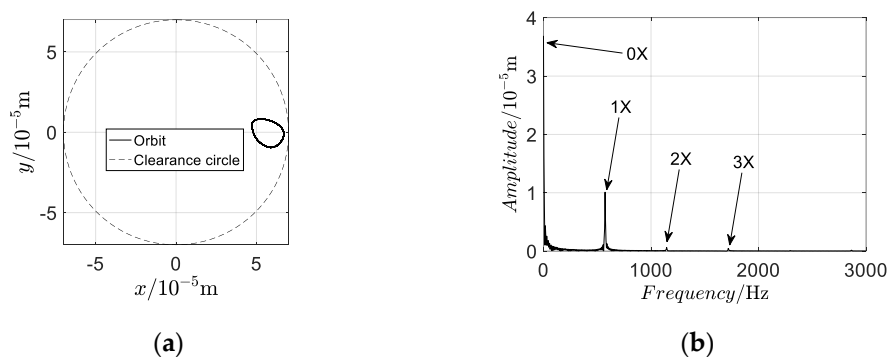


Figure 15. Orbit and spectrum of support I with $e_2 = 0.1$ mm, $e_{sx} = 0.35$ and $\omega_1 = 3600$ rad/s: (a) orbit; (b) spectrum.

3.5. Validation with Experiment Results

The rotor model from Reference [22] is modeled to validate the method presented in Section 2. Detailed configurations of the rotor system can be found in Reference [22].

The rotor model diagram is shown in Figure 16. This test rig is used to study the dynamic characteristics of a co-rotating and counter-rotating dual-rotor system with four or five supports. The additional supports in Figure 16 are removed because this paper focuses on a four-support counter-rotating dual-rotor system. The rotor system consists of four supports and four discs, of which each rotor has two discs. Each shaft is driven by a separate motor, so the rotation speed of the inner and outer rotors can be different with a speed ratio of -1.65 . The angular acceleration for the inner rotor during run-up and run-down is approximately 1.05 rad/s . The operational ranges for the inner and outer rotor are $0\text{--}232 \text{ rad/s}$ and $0\text{--}382 \text{ rad/s}$, respectively. The excitation is only due to the residual unbalance of the rotors.

Figure 17 is the counter-rotating coaxial system in this paper. The model parameters of the rotor system are listed in Tables 4–8 contains the geometric dimensions and information in each test. Table 5 contains the stiffness coefficients of the elastic supports. Tables 6 and 7 show the parameters of the intermediate bearing and SFDs. Table 8 shows the unbalanced configuration and inertia properties of each disk.

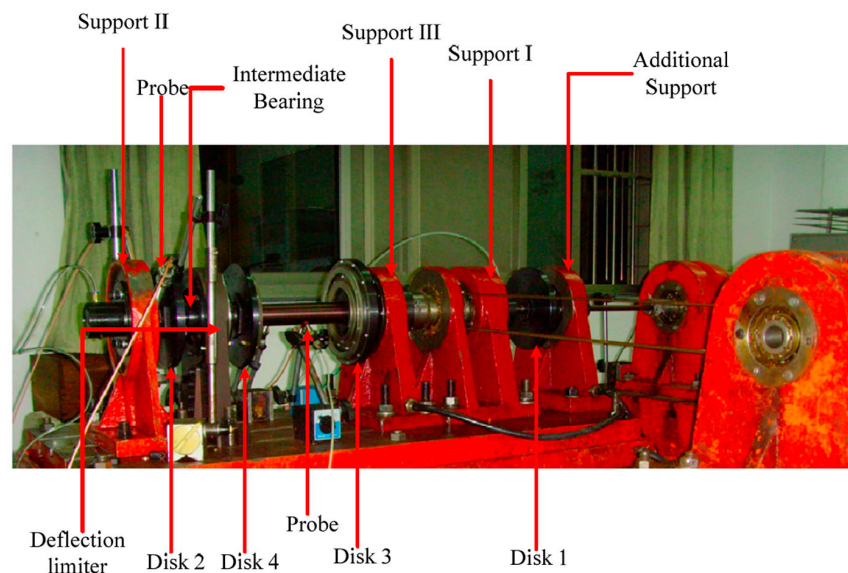


Figure 16. Dual-rotor test rig.

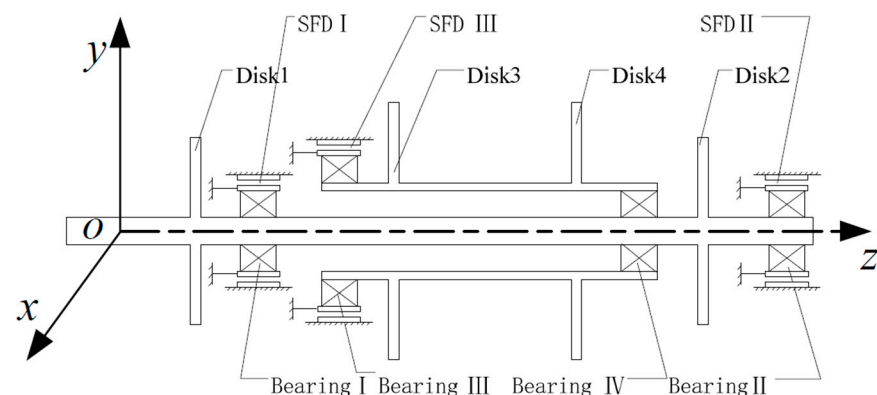


Figure 17. Structural diagram of the coaxial rotor system.

Table 4. Dimension and elements information of the rotor system.

Node No.	Axial Location (m)	Bearing/Disk	Element No.	Outer Diameter (m)	Inner Diameter (m)
1	0		1	0.018	0.00
2	0.08143		2	0.018	0.00
3	0.16286		3	0.018	0.00
4	0.24429		4	0.018	0.00
5	0.24909		5	0.018	0.00
6	0.25479		6	0.018	0.00
7	0.28879		7	0.018	0.00
8	0.32279		8	0.018	0.00
9	0.35879	Disk no.1	9	0.018	0.00
10	0.38369		10	0.018	0.00
11	0.40859		11	0.018	0.00
12	0.43349		12	0.018	0.00
13	0.43869	Bearing no.1	13	0.018	0.00
14	0.44479		14	0.022	0.00
15	0.54752		15	0.022	0.00
16	0.65025		16	0.022	0.00
17	0.75298		17	0.022	0.00
18	0.85571		18	0.022	0.00
19	0.95844		19	0.022	0.00
20	1.06117		20	0.022	0.00
21	1.06517	Bearing no.4	21	0.022	0.00
22	1.06867		22	0.022	0.00
23	1.08867		23	0.022	0.00
24	1.10867	Disk no.2	24	0.022	0.00
25	1.14274		25	0.022	0.00
26	1.17681		26	0.022	0.00
27	1.21088		27	0.017	0.00
28	1.21488	Bearing no.2	28	0.014	0.00
29	1.21838		29	0.014	0.00
30	1.23038		End of inner rotor		
31	0.64200		30	0.035	0.03
32	0.66065		31	0.035	0.03
33	0.67930	Bearing no.3	32	0.035	0.03
34	0.68650		33	0.038	0.03
35	0.71170		34	0.038	0.03
36	0.73690		35	0.038	0.03
37	0.76210	Disk no.3	36	0.038	0.03
38	0.80784		37	0.038	0.03
39	0.85358		38	0.038	0.03
40	0.89932		39	0.038	0.03
41	0.94506		40	0.038	0.03
42	0.99080	Disk no.4	41	0.038	0.03
43	1.01430		42	0.038	0.03
44	1.02030		43	0.070	0.03
45	1.03330		44	0.060	0.03
46	1.06030		45	0.060	0.03
47	1.06430	Bearing no.4	46	0.060	0.03
48	1.07380				

Table 5. Stiffness of elastic supports (squirrel cage) in the test rotor system.

	Support I	Support II	Support III	Support IV
Stiffness (N/m)	1.45×10^6	2.21×10^5	9.29×10^5	

Table 6. Parameters of the intermediate bearing in the test rotor system.

Radius of Inner Ring (mm)	Radius of Outer Ring (mm)	No. of Rollers	Contact Stiffness (N/m ^{3/2})	Radial Clearance (μm)
9.37	14.13	9	7.055×10^9	6

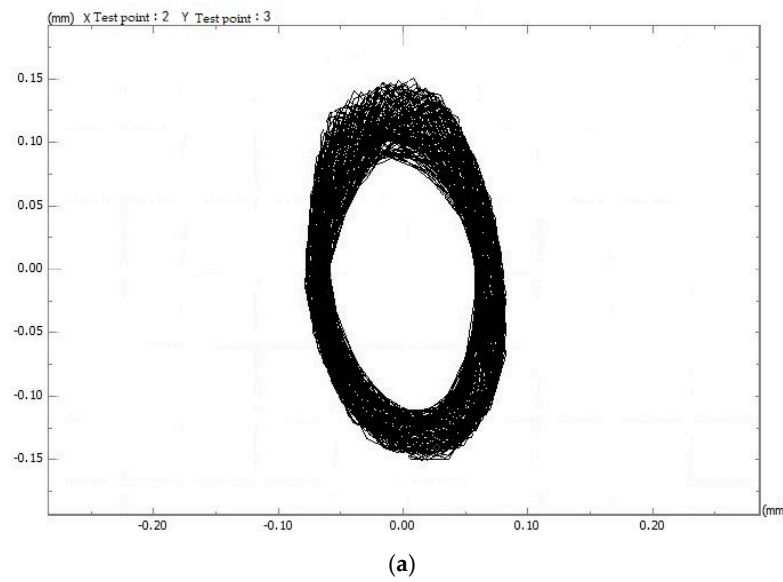
Table 7. Parameters of SFDs in the test rotor system.

	Inner Rotor Support I	Support II	Outer Rotor Support III
Radius R/mm	25	18	35
Length L/mm	15	15	20
Radial clearance c/mm	0.1	0.1	0.08
Dynamic viscosity $\mu\text{s}/10^{-2}\text{Pa}\cdot\text{s}$		1.0752	

Table 8. Unbalanced configuration and inertia properties of disks.

	Inner Rotor Disk 1	Disk 2	Outer Rotor Disk 3	Disk 4
Unbalance ($\times 10^{-5} \text{ kg}\cdot\text{m}^2$)	2	4	1	2
Mass (kg)	2.3386	2.3386	3.2590	1.6303
Polar moment of inertia ($\text{kg}\cdot\text{m}^2$)	0.00815	0.00815	0.01561	0.00661

Figure 18 is borrowed from Reference [22] for comparison with the results obtained by the method in this work, which can be seen in Figure 7. By comparing Figures 18 and 19, it can be seen that the numerical results of this work show a great agreement with those in Reference [22], which has demonstrated the validity of the method presented in this paper.

**Figure 18.** Cont.

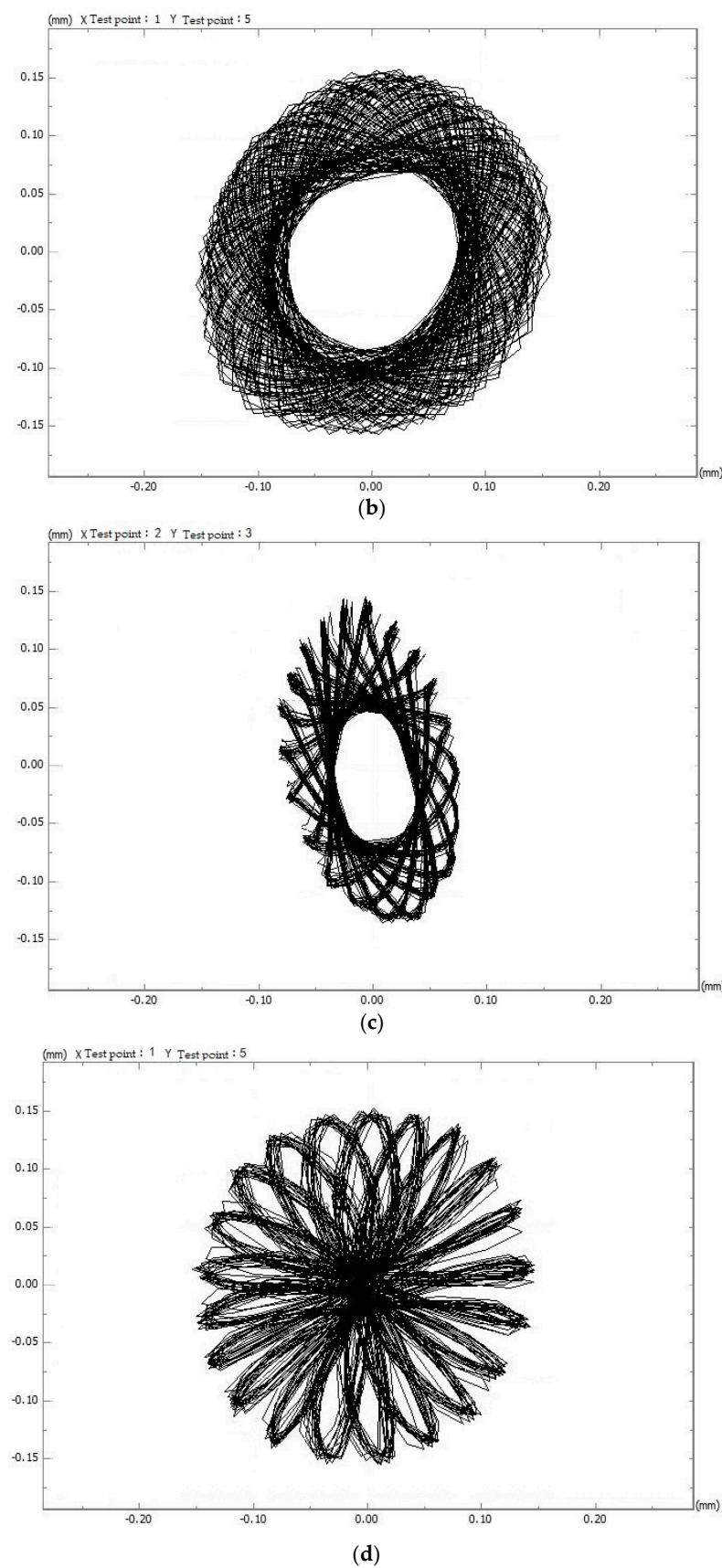


Figure 18. Experimental results from Reference [22] (Chapter 5, Figure 5.25): (a) orbit of the inner rotor disk – $\omega = 188 \text{ rad/s}$; (b) orbit of the outer rotor disk – $\omega = 188 \text{ rad/s}$; (c) orbit of the inner rotor disk – $\omega = 230 \text{ rad/s}$; (d) orbit of the outer rotor disk – $\omega = 230 \text{ rad/s}$.

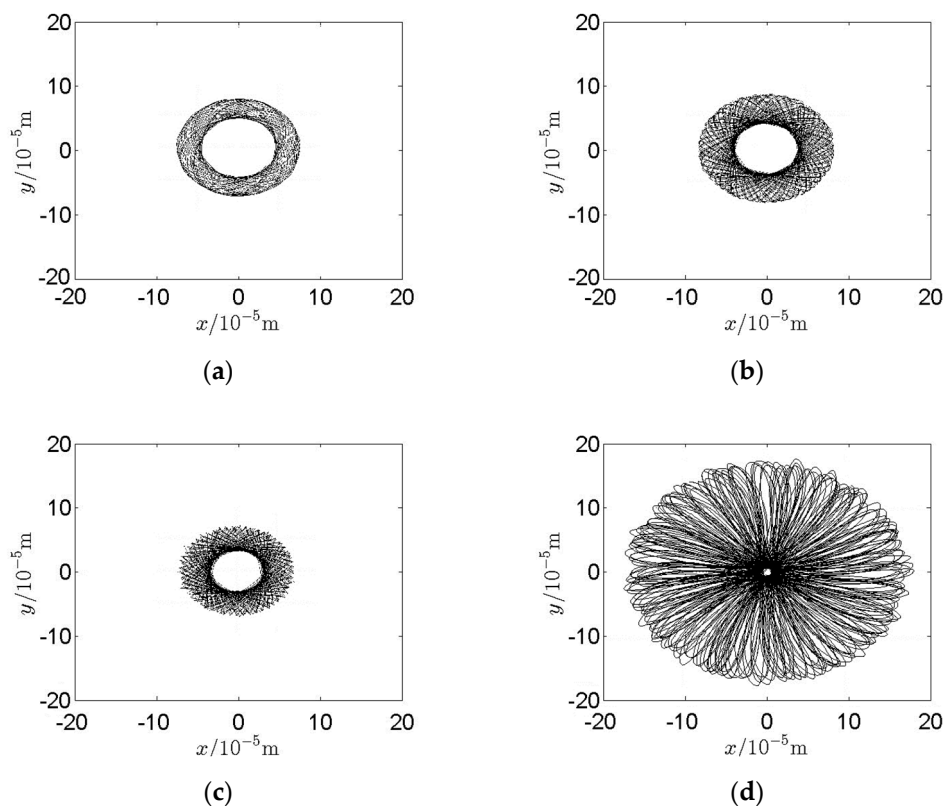


Figure 19. Results obtained with method in this work: (a) orbit of the inner rotor disk – $\omega = 188 \text{ rad/s}$; (b) orbit of the outer rotor disk – $\omega = 188 \text{ rad/s}$; (c) orbit of the inner rotor disk – $\omega = 230 \text{ rad/s}$; (d) orbit of the outer rotor disk – $\omega = 230 \text{ rad/s}$.

4. Conclusions

A recently developed time domain technique has been applied to an industrial turbine engine fitted with squeeze film dampers to study the nonlinear dynamic characteristics of the rotor system and the influence of static eccentric SFDs. The conclusions are listed below:

- (1) The periodicity of the motion of the rotor system is prone to be affected by the static sprung eccentricity. Without the sprung eccentricity, the rotor would execute periodic orbital motion under different unbalanced configurations. However, the jump phenomenon can be observed when $e_4 \geq 0.7 \text{ mm}$. With sprung eccentricity, obvious bifurcation, which indicates non-periodic motion, can be observed from the bifurcation diagram.
- (2) Due to the nonlinearity of the SFDs, the rotational speed at which the peak response occurs can be different from the critical speeds identified from the Campbell diagram. The peak response speed range would shift under different unbalanced configurations.
- (3) The operating deflection shape of the rotor system at a continuous operating speed of 3663 rad/s is strongly influenced by the amount and the axial position of the unbalance. This indicates that the response of the rotor system is much more sensitive to the unbalance of compressor II than compressor IV.
- (4) The static sprung eccentricity would lead to the occurrence of the $0X$ and $2X$ frequency components in the waterfall diagram. The amplitude of the $1X$ component increases as the amount of balance increases, while that of the $0X$ component decreases. The larger the static sprung eccentricity, the larger the amplitude of $0X$, $1X$ and $2X$.
- (5) The further the distance between the components of the rotor and the static eccentric SFD, the less affected the components are by the static eccentricity of the SFD.
- (6) Due to the static sprung eccentricity, the center for the orbit of support I would be offset from the center of the SFD and thus make the SFD inefficient/ineffective or even lead to the occurrence of rub impact.

Therefore, we propose to improve the structure of the spring butt-bearing seat and add a centering surface between them. The thickness of the spokes of the cage in the vertical direction can also be optimized to reduce the influence of the rotor's own gravity.

Author Contributions: Conceptualization, S.Z. and F.W.; methodology, S.L.; software, F.W.; validation, F.W., X.M. and Y.L.; formal analysis, S.L.; investigation, S.Z. and F.W.; resources, F.W.; data curation, X.L.; writing—original draft preparation, S.L.; writing—review and editing, S.Z. and S.L.; visualization, X.L.; project administration, X.M. All authors have read and agreed to the published version of the manuscript.

Funding: This research was funded by the Jiangxi Provincial Natural Science Foundation grant number 20202BAB211005 and the Aero Science Foundation of China grant number 201928056001.

Institutional Review Board Statement: Not applicable.

Informed Consent Statement: Not applicable.

Data Availability Statement: The data presented in this study are available on request from the corresponding author. Data are unavailable due to privacy.

Conflicts of Interest: The authors declare no conflict of interest.

References

1. Tonnesen, J. Experimental Parameter Study of a Squeeze Film Bearing. *J. Lubr. Technol.* **1976**, *98*, 206–213. [[CrossRef](#)]
2. Sykes, J.E.H.; Holmes, R. The Effects of Bearing Misalignment on the Nonlinear Vibration of Aero-engine Rotor-Assemblies. *J. Aerosp. Eng.* **1991**, *204*, 83–99.
3. Zhao, J.Y.; Linnett, I.W.; Mclean, L.J. Subharmonic and Quasi-Periodic Motions of an Eccentric Squeeze Film Damper-Mounted Rigid Rotor. *J. Vib. Acoust.* **1994**, *116*, 347–363. [[CrossRef](#)]
4. Bonello, P.; Brennan, M.J.; Holmes, R. A Study of the Nonlinear Interaction Between an Eccentric Squeeze Film Damper and an Unbalanced Flexible rotor. *J. Eng. Gas Turbine Power* **2004**, *126*, 855–866. [[CrossRef](#)]
5. Giovanni, A.; Lelio, D.P. Experimental Study of a Squeeze Film Damper with Eccentric Circular Orbits. *J. Tribol.* **2005**, *128*, 365–377.
6. Deng, H.; Diao, Y.; Zhang, J.; Zhang, P.; Ma, M.; Zhong, X.; Yu, L. Three-Dimensional Identification for Unbalanced Mass of Rotor Systems in Operation. *Appl. Sci.* **2018**, *8*, 173. [[CrossRef](#)]
7. Glasgow, D.A.; Nelson, H.D. Stability analysis of rotor-bearing systems using component mode synthesis. *J. Mech. Design.* **1980**, *102*, 352–359. [[CrossRef](#)]
8. Gupta, K.; Gupta, K.D.; Athre, K. Unbalance response of a dual rotor system: Theory and experiment. *J. Vib. Acoust.* **1993**, *115*, 427–435. [[CrossRef](#)]
9. Gupta, K.; Kumar, R.; Tiwari, M.; Prakash, O. Effect of rotary inertia and gyroscopic moments on dynamics of two spool aero engine rotor. *ASME* **1993**, *78897*, 1–14.
10. Wang, W.; Kirkhope, J. Component mode synthesis for multi-shaft rotors with flexible inter-shaft bearings. *J. Sound Vib.* **1994**, *173*, 537–555. [[CrossRef](#)]
11. Chiang, H.W.D.; Hsu, C.N.; Tu, S.H. Rotor-Bearing analysis for turbo machinery single- and dual-rotor systems. *J. Propul. Power.* **2004**, *20*, 1096–1104. [[CrossRef](#)]
12. Ma, L.; Wang, J.; Zhang, G. The Dynamic Characteristic of a Faulted Rotor System with Multi-Objective Optimization Designed SFD. *Appl. Sci.* **2019**, *9*, 3628. [[CrossRef](#)]
13. Wang, H.; Zhao, Y.; Luo, Z.; Han, Q. Analysis on Influences of Squeeze Film Damper on Vibrations of Rotor System in Aeroengine. *Appl. Sci.* **2022**, *12*, 615. [[CrossRef](#)]
14. AL-Solihat, M.K.; Behdinan, K. Force transmissibility and frequency response of a flexible shaft-disk rotor supported by a nonlinear suspension system. *Int. J. NonLin. Mech.* **2000**, *124*, 103501. [[CrossRef](#)]
15. Nan, G.; Zhang, Y.; Zhu, Y.; Guo, W. Nonlinear dynamics of rotor system supported by bearing with waviness. *Sci. Prog.* **2020**, *103*, 1–29. [[CrossRef](#)] [[PubMed](#)]
16. Zhang, H.P.; Lu, L.; Zhang, W.; Fu, C. Investigation on dynamic behaviors of rotor system with looseness and nonlinear supporting. *Mech. Syst. Signal Process.* **2022**, *166*, 108400. [[CrossRef](#)]
17. Wang, H.; Han, Q.K.; Zhou, D.N. Nonlinear dynamic modeling of rotor system supported by angular contact ball bearings. *Mech. Syst. Signal Process.* **2017**, *85*, 16–40. [[CrossRef](#)]
18. Iskakov, Z.; Nutpulla, J.; Bissembayeb, K.; Kamal, A. Dynamic modeling of a non-ideal gyroscopic rotor system with nonlinear damping and nonlinear rigidity of an elastic support. *Adv. Mech. Eng.* **2022**, *14*, 1–31. [[CrossRef](#)]
19. Li, S.; Lu, Y.; Zhang, Y.; Luo, H.; Wang, S.; Kan, X. Nonlinear dynamic response and bifurcation of asymmetric rotor system supported in axial-grooved gas-lubricated bearings. *J. Low Freq. Noise Vib. Act. Control* **2021**, *41*, 451–478. [[CrossRef](#)]

20. Zhou, H.L.; Luo, G.H.; Chen, G.; Wang, F. Analysis of the nonlinear dynamic response of a rotor supported on ball bearings with floating-ring squeeze film dampers. *Mech. Mach. Theory* **2013**, *59*, 65–77. [[CrossRef](#)]
21. Wang, F.; Luo, G.-H.; Yang, X.-G.; Cui, H.-T. Research on modeling and dynamic characteristics of complex coaxial rotor system. *J. Vibroeng.* **2017**, *19*, 1524–1545. [[CrossRef](#)]
22. Meng, C. Research on Influences of Supporting on Dynamic Characteristics of the Dual-rotor system. Master’s Thesis, Nanjing University of Aeronautics and Astronautics, Nanjing, China, 2014.

Disclaimer/Publisher’s Note: The statements, opinions and data contained in all publications are solely those of the individual author(s) and contributor(s) and not of MDPI and/or the editor(s). MDPI and/or the editor(s) disclaim responsibility for any injury to people or property resulting from any ideas, methods, instructions or products referred to in the content.